

MATERIALS SCIENCE

Ultrapermeable 2D-channelled graphene-wrapped zeolite molecular sieving membranes for hydrogen separation

Radovan Kukobat^{1,2}, Motomu Sakai³, Hideki Tanaka¹, Hayato Otsuka¹, Fernando Vallejos-Burgos^{1,4}, Christian Lastoskie⁵, Masahiko Matsukata^{3,6,7}, Yukichi Sasaki⁸, Kaname Yoshida⁸, Takuya Hayashi⁹, Katsumi Kaneko^{1*}

Copyright © 2022
The Authors, some
rights reserved;
exclusive licensee
American Association
for the Advancement
of Science. No claim to
original U.S. Government
Works. Distributed
under a Creative
Commons Attribution
License 4.0 (CC BY).

The efficient separation of hydrogen from methane and light hydrocarbons for clean energy applications remains a technical challenge in membrane science. To address this issue, we prepared a graphene-wrapped MFI (G-MFI) molecular-sieving membrane for the ultrafast separation of hydrogen from methane at a permeability reaching 5.8×10^6 barrers at a single gas selectivity of 245 and a mixed gas selectivity of 50. Our results set an upper bound for hydrogen separation. Efficient molecular sieving comes from the subnanoscale interfacial space between graphene and zeolite crystal faces according to molecular dynamic simulations. The hierarchical pore structure of the G-MFI membrane enabled rapid permeability, indicating a promising route for the ultrafast separation of hydrogen/methane and carbon dioxide/methane in view of energy-efficient industrial gas separation.

INTRODUCTION

H₂ is a notable industrial target for clean energy generation and intensive CO₂ reduction (1, 2), and it is mainly produced through steam reforming of natural gas (3). The energy-saving recovery of H₂ from refinery streams containing H₂, CH₄, and light hydrocarbons is ultimately aimed at consistently reducing CO₂ emissions (2, 4). The recovery of H₂ from refinery gases via membrane separation is more favorable than distillation with regard to energy consumption and reduction of CO₂ emissions (5–7). The steam reforming process of natural gas is performed at a high temperature of approximately 1000 K (3); thus, thermally stable membranes are preferred for an energy-saving process.

Zeolite membranes are thermally stable and robust and are promising candidates for application in the steam reforming process. However, zeolites with small pores pose a challenge because their pore sizes are larger than the molecular size of CH₄. MFI zeolites with a uniform pore size of 0.55 nm (8) are suitable candidates for membrane fabrication and have been extensively studied for high-performance separation processes. Recent study of membranes has reported progress in MFI zeolite membranes in which crack-free MFI membranes were prepared using exfoliated MFI nanosheets (9). However, the pore sizes of the MFI membranes are larger than the molecular sizes of the target H₂ and CH₄; therefore, the selectivity of H₂/CH₄ was limited to 25 (10). Although the crack

issue in zeolite membranes is addressed by the development of a layered zeolite membrane route, the establishment of an energy-saving separation technology requires a new type of thermally stable zeolite-based membrane that enables the rapid and selective separation of H₂ from CH₄ or other gases.

Therefore, the development of outstanding zeolite-based membranes for the construction of H₂-assisted green technology is an active challenge (11). Internal surface modification of MFI zeolite channels reduces the effective size of the channels, achieving a H₂/CH₄ selectivity of 74 with H₂ permeance of 4.9×10^{-8} mol m⁻² s⁻¹ Pa⁻¹ at 300 K (12) and a H₂/CO₂ selectivity of 25 with H₂ permeance of 1.28×10^{-7} mol m⁻² s⁻¹ Pa⁻¹ at 723 K (13). Mixed matrix membranes (MMMs) consisting of zeolites and other porous fillers have been explored as high-performance membranes (14, 15). A hollow silicalite-1 (MFI) MMM exhibited a H₂/CH₄ selectivity of 180 at a permeance of $\sim 10^{-8}$ mol m⁻² s⁻¹ Pa⁻¹ at 300 K (16). Nevertheless, the performance of MMMs is still inadequate, and the development of membranes with high permeance and concurrent high selectivity is crucial. In comparison to polymer-based membranes, inorganic porous membranes can achieve the aforementioned properties (17). This study focused on the development of zeolite-based membranes as a class of inorganic membranes.

A promising solution consists of using a membrane made of small zeolite crystals wrapped with colloidal graphene sheets bearing nanoscale holes (nanowindows) (18, 19). Target gases permeate through the nanowindows (20) and access the interfacial spaces between graphene and zeolite crystal surfaces. The graphene-graphene attractive interactions are the strongest per weight because of the densely packed carbon atoms in the graphene structure (21). Consequently, the graphene-wrapped zeolite particles adhere to each other through face-to-face and/or edge-shared contacts via van der Waals interactions (22), providing a crack-free membrane through a simple compression method. The zeolite crystal faces of uneven groove structures provide a graphene-zeolite interfacial space that can sieve gases depending on their molecular sizes.

If the nanowindows are large enough to host the target H₂ molecules and the interfacial space between graphene and the zeolite

¹Research Initiative for Supra-Materials, Shinshu University, 4-17-1 Wakasato, Nagano 380-8553, Japan. ²Center for Biomedical Research, Faculty of Medicine, University of Banja Luka, Save Mrkalja 14, Banja Luka 78000, Bosnia and Herzegovina. ³Research Organization for Nano and Life Innovation, Waseda University, 513 Waseda-Tsurumaki-cho, Shinjuku-ku, Tokyo 162-0041, Japan. ⁴Morgan Advanced Materials, Carbon Science Centre of Excellence, 310 Innovation Blvd., Suite 250, State College, PA 16803, USA. ⁵Department of Civil and Environmental Engineering, University of Michigan, 1351 Beal Avenue, Ann Arbor, MI 48109-2125, USA. ⁶Department of Applied Chemistry, Waseda University, 513 Wasedatsurumaki-cho, Shinjuku-ku, Tokyo 162-0041, Japan. ⁷Advanced Research Institute for Science and Engineering, Waseda University, 513 Wasedatsurumaki-cho, Shinjuku-ku, Tokyo 162-0041, Japan. ⁸Nanostructures Research Laboratory, Japan Fine Ceramics Center, 2-4-1 Mutsuno, Atsuta-ku, Nagoya 456-8587, Japan. ⁹Department of Water Environment and Civil Engineering, Shinshu University, 4-17-1 Wakasato, Nagano 380-8553, Japan.

*Corresponding author. Email: kkaneko@shinshu-u.ac.jp

surface fits only H_2 molecules, then H_2 can selectively permeate through the interfacial spaces. The permeance through these graphene-zeolite interfacial channels is larger than that of the intrinsic three-dimensional (3D) interconnected MFI channels. Our experimental observations confirmed that the MFI crack-free membrane (23, 24) exhibited a H_2 permeance of $3.6 \times 10^{-7} \text{ mol m}^{-2} \text{ s}^{-1} \text{ Pa}^{-1}$ and a H_2/CH_4 selectivity of 1.41, whereas the graphene-MFI interfacial space channelled membrane exhibited a permeance of $1.3 \times 10^{-5} \text{ mol m}^{-2} \text{ s}^{-1} \text{ Pa}^{-1}$ and a H_2/CH_4 selectivity of 245. Thus, the process of wrapping can create subnanoscale graphene-zeolite interfacial channels that are smaller than intrinsic zeolite channels (that is, 0.55 nm for MFI) and beneficial for energy-saving ultrafast separation. Introducing a hierarchical pore structure in the membrane by controlling the aggregation structure of the graphene-wrapped zeolite particles enhanced the permeance of the membrane. For smaller zeolite crystal sizes, shorter paths were formed; thus, the permeance in the interfacial spaces further increased. The apparent thickness of the graphene-wrapped MFI (G-MFI) membranes reached hundreds of micrometers. However, the G-MFI membrane with a large intergranular porosity enabled the high permeance; the effective permeation length of the graphene-MFI interface, which determines the permeation rate, should be extremely small in comparison with the apparent thickness of the G-MFI membrane, as suggested elsewhere (25, 26). Furthermore, the graphene-wrapped zeolite membranes provided sufficient thermal stability because the colloidal graphene produced from graphene oxides (GOs) was stable up to 600 K (27). In this study, MFI zeolites were used owing to the intrinsic surface groove structure (28) that turned into the interfacial channels available for molecular sieving upon wrapping. The ultrafast and highly selective permeation of H_2 through a G-MFI zeolite membrane was reported.

RESULTS

G-MFI membrane and separation efficiency

G-MFI crystals were prepared via a colloidal method on the basis of tuning the surface charges of GO and MFI crystals with NH_4Cl (fig. S1, A to C). The GO-wrapped MFI crystals were thermally treated to reduce GO to graphene in an Ar atmosphere and were thermally stable, as confirmed by thermogravimetric analysis and Raman spectroscopic analyses (fig. S1, D to F). The thermogravimetric curve shows distinctive weight losses at 440 and 746 K owing to the thermal reduction of GO and burning of the reduced graphene. Raman spectroscopy indicates a D/G intensity ratio against temperature almost constant up to 623 K, providing that the structure of graphene on MFI is not altered upon thermal treatment in air, thus denoting the thermal stability of the G-MFI membrane. The membranes (0.6 cm by 0.6 cm) were prepared by compression of crystalline and spherical G-MFI powders at 550 MPa (fig. S1, G to J).

As shown in Fig. 1A, the G-MFI membranes exhibit an outstanding H_2 permeability compared to metallic-organic frameworks (MOFs) and other zeolitic membranes, ascribable to the highly microporous and mesoporous structure. The graphene layers wrapped the MFI crystals (Fig. 1B), enabling the facile production of a crack-free MFI membrane, as confirmed by scanning electron microscopy (SEM) and permeation experiments. Furthermore, the SEM image of the G-MFI membranes surface shows the presence of intergranular mesoscale pores in the crystal assemblies, produced by freeze-drying. These pores are also visible in the cross-sectional view of the fractured

G-MFI membranes (Fig. 1C). The cross-sectional SEM image shows a sheet-like structure, consisting of mutually combined G-MFI particles. The sheet-like structures were firmly stacked with each other in the thickness direction. The G-MFI particles were slightly dispatched from the stacked layer structure, because of fracturing of the G-MFI membrane. Therefore, the cross-sectional SEM image confirms a membrane film formation consisting of continuous graphene-wrapped zeolite particles.

The G-MFI membrane was further investigated using transmission electron microscopy (TEM) (Fig. 1, D and E). MFI has a highly crystalline structure, with elliptically shaped micropores (0.55 nm), which are visible at the (010) crystal faces (fig. S2). Partial edge contact between the G-MFI crystals was observed using TEM (Fig. 1, C and E). The graphene layers allowed adherence among the MFI crystals, suppressing intergranular crack formation. Moreover, the TEM images show the presence of nanowindows in the graphene used to wrap the MFI crystals (Fig. 1E and fig. S3). The MFI particles were wrapped with a few layers of graphene (fig. S4, A to C). The hexagonal structure of G-MFI was clearly observed using inverse Fourier transform images (fig. S4, D to L). The nanowindows, characterized by a cross-sectional area in the range of 0.3 to 7.4 nm² (Fig. 1F), are wider than the permeate molecules, whose molecular size ranges from 0.26 to 0.55 nm, suggesting a preferential path for gas diffusion.

Density measurement supported the G-MFI membrane formation, with edge-shared 3D porous structures (cross section shown in Fig. 1G). The G-MFI membrane void volume fraction (0.29) was determined from the ratio between the G-MFI membrane bulk density (1.25 g cm^{-3}) and the MFI bulk density (1.76 g cm^{-3}) (8). This value indicates the presence of intergranular voids, which enable very rapid permeation. The diffusion coefficient of H_2 through the G-MFI membrane was determined to be $9.5 \times 10^{-2} \text{ cm}^2 \text{ s}^{-1}$ by approximation using solution diffusion transport (see Supplementary Text). The diffusion coefficient of CH_4 was $1.1 \times 10^{-4} \text{ cm}^2 \text{ s}^{-1}$, and thus, the ratio of the H_2 and CH_4 diffusion coefficients gives a diffusivity selectivity of H_2/CH_4 as high as 850. On the contrary, the ratio of the solubility coefficients of $2.0 \times 10^{-4} \text{ mol m}^{-3} \text{ Pa}^{-1}$ for H_2 and $7.5 \times 10^{-4} \text{ mol m}^{-3} \text{ Pa}^{-1}$ for CH_4 yielded a solubility selectivity of 0.27. The solubility selectivity slightly affects the diffusivity selectivity, as suggested by eq. 2 in Supplementary Text, indicating that the predominant separation mechanism of G-MFI originates from the diffusion mechanism, not from the solubility mechanism. This is because G-MFI has definite geometrical nanoscale spaces between the graphene and MFI crystal faces, which can discern H_2 from CH_4 . The diffusion of H_2 through the G-MFI membrane is three orders of magnitude higher than that through liquid water ($4.5 \times 10^{-5} \text{ cm}^2 \text{ s}^{-1}$) (29). This agrees with the high void fraction of 0.29 of the G-MFI membrane, as shown in the model (Fig. 1G). Figure 1H shows the key model structure of narrow graphene-zeolite interfacial channels for excellent selectivity, which was further confirmed by the molecular dynamics (MD) simulation described later.

Adsorption

The porosity of both G-MFI powder and membrane were determined by N_2 adsorption at 77 K (Fig. 2). The N_2 adsorption isotherm shows a high uptake by micropores in the low P/P_0 region. The hysteresis loop over the range $0.10 < P/P_0 < 0.15$ (Fig. 2A) arises from the in-pore phase transition of adsorbed N_2 due to intensive confinement (30, 31). A lower pressure shift is observed at the in-pore

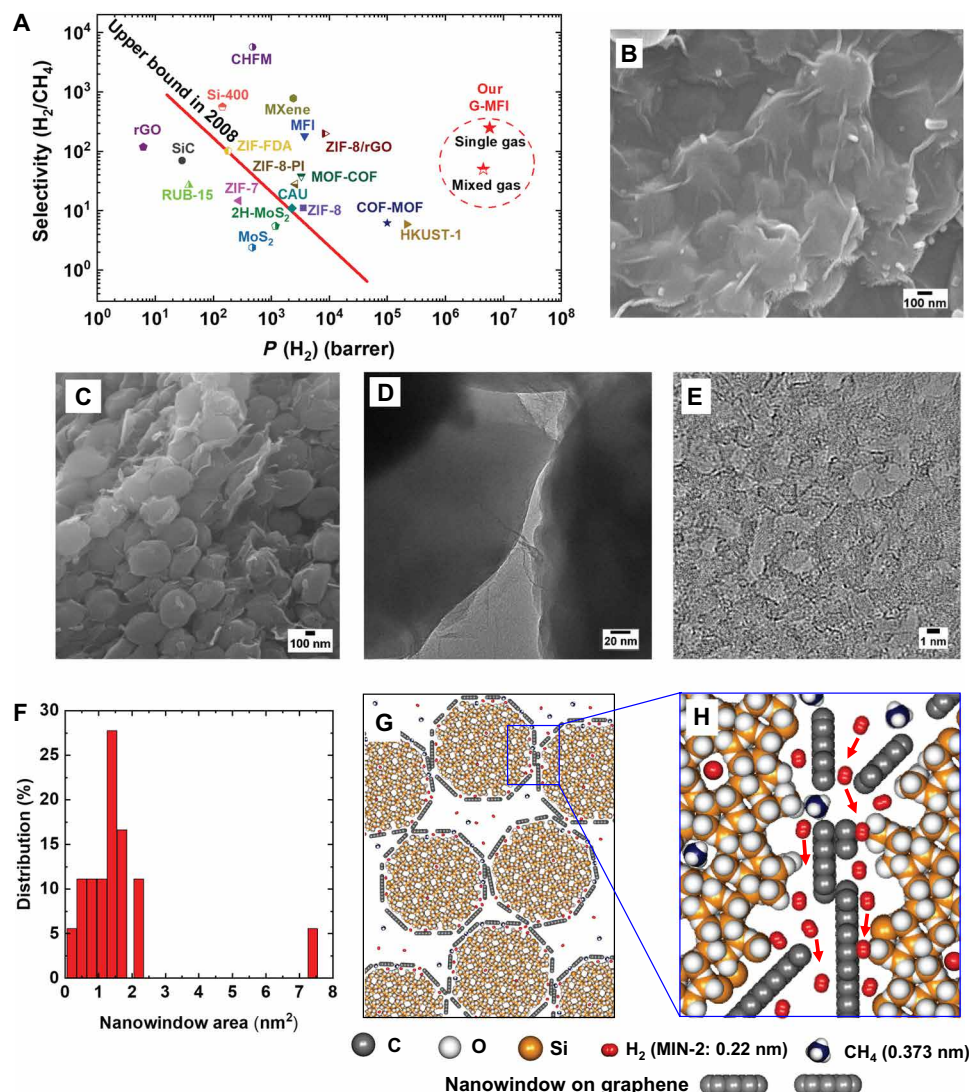


Fig. 1. H₂/CH₄ separation efficiency achieved with G-MFI. (A) Robeson plot for H₂/CH₄ separation for single gas separation. For G-MFI membranes, the selectivity of both single and mixed gas is indicated. The red line refers to the upper bound proposed by Robeson using polymeric membranes (44). Robeson plot details are listed in table S1. (B) G-MFI SEM image. (C) Fractured G-MFI SEM cross-sectional image. (D) TEM image highlighting the contact between two MFI crystals wrapped with graphene. (E) TEM image of nanowindows in graphene. (F) Nanowindow size distribution histogram. (G) Edge share model structure of G-MFI membrane, depicting intergranular voids; the (010) crystallographic face of MFI is shown. (H) Simplified interfacial model showing the cross-sectional view of the graphene and MFI crystal face of the G-MFI membrane. The nanowindows in the single graphene layer are expressed by blanks in the graphene layer, although a graphene layer continuously covers the zeolite crystal. TEM images show a few graphene layers with nanowindows covering an MFI zeolite crystal in the real G-MFI (fig. S4). Few-layer wrapping can be approximated with monolayer wrapping because the gas permeance between the layers is negligible.

phase transition point. The reason for the shift is reasonably associated with a slight distortion of the MFI lattice during the graphene-wrapping and freeze-drying procedures, as indicated by the change in the full width at half maximum of the x-ray diffraction peaks (fig. S5A and table S2). The logarithmic plots of MFI and G-MFI powder (inset of Fig. 2A) show comparable N₂ adsorption uptakes in the low-pressure region, suggesting that microporosity is preserved after graphene wrapping.

In contrast, the N₂ adsorption isotherms of the G-MFI membrane at 77 K are remarkably different from those of the MFI membrane. In particular, the N₂ adsorption amount is higher for G-MFI membrane (Fig. 2B). The enhanced uptake below $P/P_0 = 0.1$ on the

G-MFI membrane indicates the formation of very small micropores by wrapping procedure. The obtained micropores mainly originate from the interfacial space between graphene and MFI crystals, resulting in a slight increase in microporosity (table S3). The N₂ adsorption isotherm related to the interfacial space was obtained by subtraction of the N₂ adsorbed amount of G-MFI from that of the MFI membrane (fig. S6A). The pore size distribution obtained from the subtracted isotherm by quenched solid density functional theory for slit pores shows the presence of different pore sizes. Micropores are assigned to the interfacial space between graphene and MFI, whereas mesopores (3.8 to 6.0 nm) originate from the mutually aggregated structure of G-MFI particles, both in compression

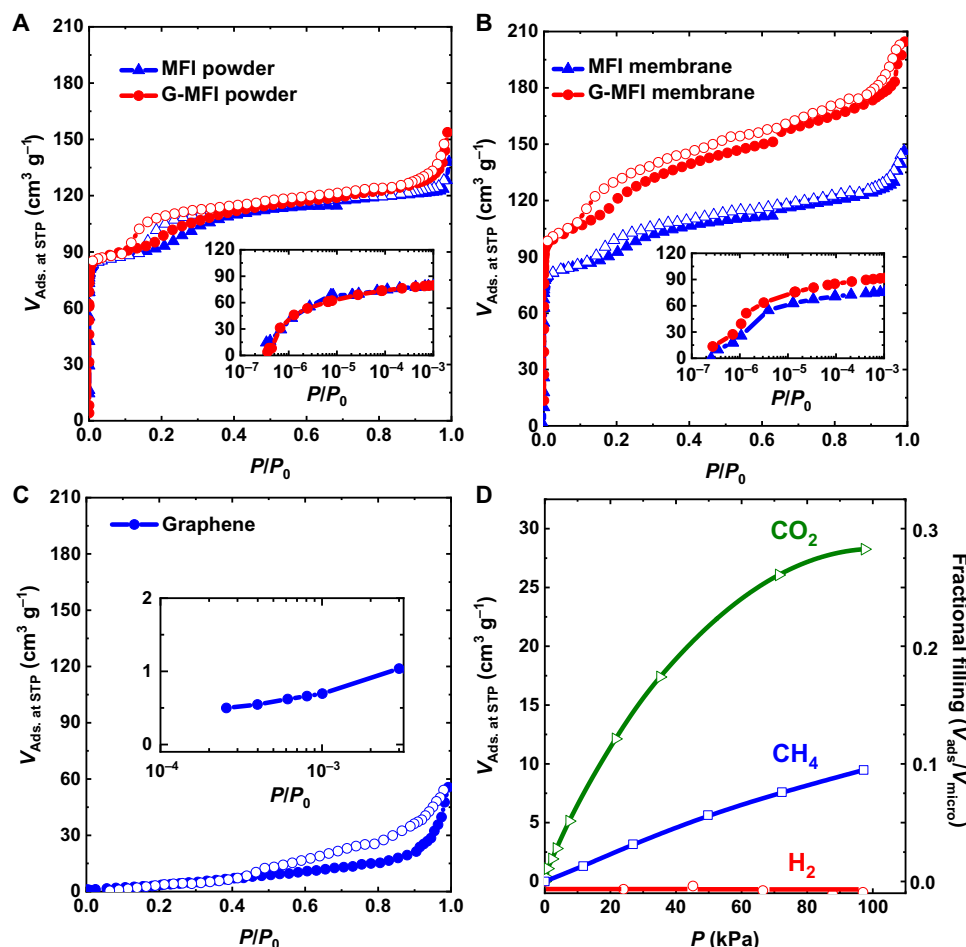


Fig. 2. Porosity of G-MFI membranes as determined from N₂ adsorption at 77 K. (A) N₂ adsorption (Ads.) isotherms of G-MFI and MFI powder. Inset is the corresponding semilogarithmic plot. STP, standard temperature and pressure. (B) N₂ adsorption isotherms of G-MFI and MFI membrane. Inset is the corresponding semilogarithmic plot. (C) N₂ adsorption isotherm of compressed graphene. Inset is the corresponding semilogarithmic plot. (D) Adsorption isotherms and fractional fillings of H₂, CO₂, and CH₄ plotted against pressure. The density of liquid H₂ (0.0711 g cm⁻³ at 20 K and 10⁵ Pa), solid CO₂ (1.566 g cm⁻³ at 193 K and 10⁵ Pa), and liquid CH₄ (0.423 g cm⁻³ at 111 K and 10⁵ Pa) and micropore volume (table S3) of the G-MFI membrane were used to estimate the fractional fillings.

direction and plane direction (fig. S6B). Micropore and mesopore wide distribution suggests the presence of a hierarchical pore structure, which plays a prominent role in rapid permeation. **Experimental micropore volume estimated from the subtracted G-MFI isotherm at 77 K, related to the adsorption at the interfacial space, was 0.02 cm³ g⁻¹. This value indicates the presence of the narrow interfacial space available for the gas permeation.** The theoretical graphene-MFI interfacial micropore volume was calculated by subtracting the MFI model pore volume from the G-MFI model pore volume. The obtained value of 0.03 ml g⁻¹ is comparable with the experimental result, confirming the validity of the proposed G-MFI model (Fig. 1, G and H). The presence of intergranular micropores was also confirmed by the fact that small-angle x-ray scattering intensity of the G-MFI membrane is larger than that of MFI crystals (fig. S5, B and C). We estimated gyration radii (R_g) from the linear region of Guinier plots (fig. S5C), considering the requirement ($QR_g < 1.3$) for fitting. The R_g of the G-MFI membrane is smaller than that of the MFI membrane, thereby suggesting a decrease in the size of micropores by graphene wrapping (table S4). The R_g of 0.48 nm suggests the presence of intergranular voids in the G-MFI membrane.

The G-MFI particles were more mutually contacted than the compressed MFI membrane without graphene wrapping. Therefore, we assume that the graphene on the MFI crystal contributes to the crack-free membrane formation. In contrast, the strong graphene-graphene interaction suppressed the formation of micropores between adjacent G-MFI crystals, as shown by the adsorption amount below $P/P_0 = 0.1$ (Fig. 2C).

The average micropore width of the interfacial space between graphene and the MFI crystal face was estimated to be ~0.40 nm, assuming the presence of slit-shaped micropores (32). However, N₂ adsorption cannot evaluate the exact pore widths that are less than ~0.40 nm owing to the pore blocking effect. The width of the interfacial space, which induces the molecular sieving effect shown later, should be less than ~0.40 nm. The MD study further introduced provides reliable information about the interfacial space structure for molecular sieving.

Figure 2D reports the adsorption of the target gases adopted for separation, namely, H₂, CH₄, and CO₂, on the G-MFI membranes. The supercritical H₂ was not adsorbed. Supercritical CH₄ interacts more strongly with micropores than H₂, giving rise to considerable

adsorption. In contrast, subcritical CO₂ with a large quadrupole moment can strongly interact with the micropores (33), leading to a more adsorption than CH₄. The fractional fillings of pores by adsorbed CO₂ and CH₄ were approximately 0.3 and 0.1, respectively (Fig. 2D). Consequently, the selectivity of H₂ against CO₂ or CH₄ using their mixed gases is reasonably smaller, due to the interaction of H₂ with adsorbed CO₂ or CH₄ as discussed later on for H₂/CH₄ mixed gas separation.

Permeability

The G-MFI membrane separation ability was investigated by gas permeability measurements with H₂, He, CO₂, N₂, CH₄, i-C₄H₁₀, and SF₆, whose molecular size ranges from 0.26 nm for He to 0.55 nm for SF₆. As shown in Fig. 3A, the permeability decreased with molecular size from H₂ to CH₄. H₂ has a higher permeability than He because the molecular size of diatomic H₂ [second minimum dimension (MIN-2): 0.22 nm] is smaller than that of He (MIN-2: 0.28 nm) (34). The smaller molecular mass of H₂ compared to He also contributed to its higher permeability.

Furthermore, the selectivity of H₂ against He, CO₂, N₂, CH₄, i-C₄H₁₀, and SF₆ for the G-MFI membranes was measured, and the corresponding Robeson plot is shown in Fig. 1A. The selectivity

increased with increasing molecular size from H₂/He to H₂/CH₄ (Fig. 3B). The H₂/CH₄ selectivity reached 245. For i-C₄H₁₀ and H₂/SF₆, the permeability was too low to be confidently measured; therefore, only an indication of maximum permeability and minimum selectivity is shown in Fig. 3, A and B. The G-MFI membrane has a significantly higher selectivity for H₂ than the MFI membrane without wrapping (fig. S7). The MFI membrane contains cracks, resulting in lower H₂ selectivity and higher permeability for other gases. Thus, the interfacial micropore spaces between graphene and MFI crystal faces impart outstanding separation ability to the G-MFI membrane. An equimolar mixture of H₂/CH₄ could be efficiently separated with a selectivity of 50, and the system was stable for more than 7 days (Fig. 3C). Noticeably, the mixed-gas selectivity was lower than that of the single-gas selectivity because of the hindrance effect of adsorbed CH₄ molecules in the pores (Fig. 2D and movie S1). The decrease in H₂/CH₄ selectivity for a mixed gas is a result of an increase in CH₄ permeability from 2.3×10^4 barrers for single gas to 8.9×10^4 barrers for a mixed gas.

Figure 3D shows the Robeson plot for CO₂/CH₄ separation. The G-MFI membrane exhibits a high selectivity for CO₂ at a high permeability of 1.1×10^6 barrers and a CO₂/CH₄ selectivity of 50 that is

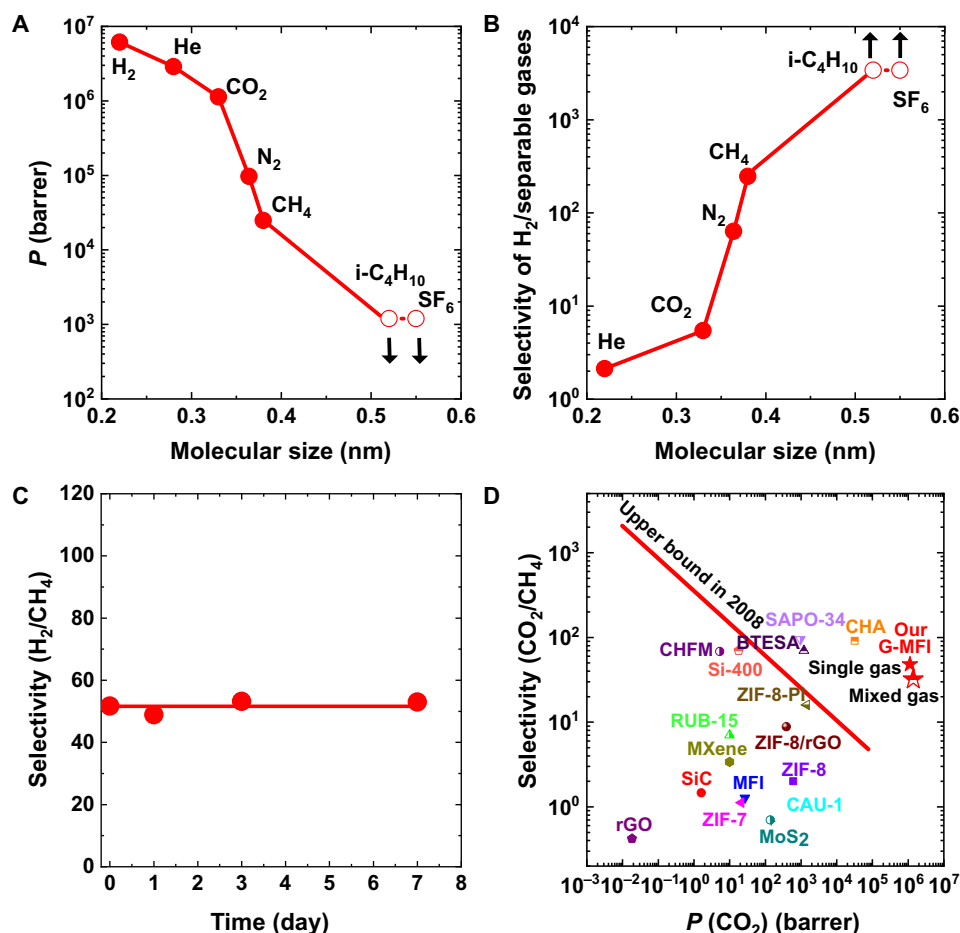


Fig. 3. Gas separation performance of G-MFI membrane. (A) Variation in single-gas permeability with molecular size for the gases H₂, He, CO₂, N₂, CH₄, i-C₄H₁₀, and SF₆. The MIN-2 molecular sizes of H₂ and He are used. (B) Selectivity of H₂ plotted against molecular size. Separable gases include He, CO₂, N₂, CH₄, i-C₄H₁₀, and SF₆. (C) Selectivity change with time for the separation of the H₂/CH₄ equimolar mixture. (D) Robeson plot for CO₂/CH₄. For the G-MFI membrane, both single and mixed gas CO₂/CH₄ selectivity is indicated for comparison. The red line shows the Robeson plot for polymeric membranes (44). Details of the Robeson plots with references are presented in table S1. The arrows in Fig. 2 (A and B) show that the permeability and selectivity for i-C₄H₁₀ and SF₆ (open symbols) are maximum and minimum values, respectively.

comparable to the CO₂/CH₄ separation using SAPO membranes (35). The CO₂ permeability was slightly higher for the mixed gas than for the single gas. The CH₄ mixed gas permeability of 4.9×10^4 barrers was higher than the single gas permeability of 2.2×10^4 barrers. Therefore, the CO₂/CH₄ selectivity decreased to 30 in the case of mixed gas steady permeability (fig. S8). The observed permeability behavior stems from the enhanced adsorption effect of the pre-adsorbed molecules (36). Both CO₂ and CH₄ were adsorbed on the pore walls of intergranular connection areas akin to the interfacial spaces, enhancing the adsorption by effectively narrowing the pores for further adsorption. As CO₂ is more preadsorbed than CH₄, CH₄ can obtain an explicit merit for permeation compared with CO₂.

Permeability mechanisms

MD simulations were further used to investigate the H₂ and CH₄ separation mechanisms (Fig. 4). MFI crystal rod models (fig. S9) of 7.885 and 43.368 nm in length along the *c* axis were used. As shown in Fig. 4A, the crystals were completely wrapped with single graphene, and nanowindows of ~1 nm in diameter were located at the left- and right-side centers, in contact with the left and the right (001) faces of the MFI crystal, as the inlet and outlet of the gases (Fig. 4B). The (010) face is predominant (fig. S2), whereas the (100) is the second predominant. Moreover, MFI crystals have straight channels (0.56 nm by 0.53 nm) along the *b* axis and sinusoidal channels (0.51 nm by 0.55 nm) along the *a* axis. These channels are terminated at the (010) and (100) crystal faces. Considering these observations, the adopted MFI crystal model showed (100) and (010) as the predominant crystal faces along the *c* axis (fig. S9). The gas permeates from the left nanowindow to the right nanowindow through the 2D interfacial space between graphene and the (010) and (100) faces of the MFI crystal rod, as indicated by the arrows in Fig. 4A. The effect of the length of the MFI crystal rod, interfacial surface area of the MFI crystal, and effective width (w_{eff}) of the 2D interfacial space on H₂ and CH₄ permeation were examined. The examined G-MFI crystal rod model was at the equilibrium interface ($w_{\text{eff}} = 0.03$ nm) between graphene and MFI crystal faces, whereas G-MFI models of $w_{\text{eff}} = 0.30$ nm and $w_{\text{eff}} = 0.40$ nm are shown in fig. S10 (A to D) for comparison. Interfacial and pore structures were significantly affected by MFI crystal surface morphology (Fig. 4, C and D). The MFI unit cell has three grooves at the (100) face, causing surface roughness and affecting interfacial pore spaces size and shape. Effective pore widths of $w_1 = 0.310$ nm, $w_2 = 0.369$ nm, and $w_3 = 0.272$ nm were observed (Fig. 4C). The interfacial spaces of w_1 and w_2 are compatible to the sole hydrogen (0.295 nm), thus giving rise to H₂ permeability. Conversely, the groove sites between graphene and the smooth (010) crystal face were too narrow ($w_4 = 0.188$ nm and $w_5 = 0.106$ nm) for H₂ and CH₄ (Fig. 4D). Therefore, the interfacial space size governs the permeation and separation of H₂ and CH₄.

H₂ and CH₄ permeation pathways through the interfacial spaces between graphene and the (001), (100), and (010) faces are indicated with arrows in Fig. 4E. H₂ permeates through the pores of MFI and interfacial spaces I, I', II, and II', providing continuous projected trajectories of H₂ along all interfacial spaces of I, I', II, and II' (Fig. 4E₁); contrarily, CH₄ (0.37 nm) only permeates through the pores and interfacial spaces of II and II', characterized by a groove structure (Fig. 4E₂). H₂ and CH₄ trajectories through the pores of MFI and interfacial spaces between graphene and the (100) faces show evidently different transport pathways for H₂ and CH₄ (Fig. 4, F₁ and F₂). The red arrows at the top and bottom interfaces along the

(100) face constitute the bold and continuous permeation pathways of H₂, in addition to intrapore permeation, leading to the observed rapid permeation and selectivity (Fig. 4F₁). CH₄ trajectory pathways show that CH₄ cannot pass through the interface between graphene and MFI crystal but only through the pores (Fig. 4F₂). CH₄ permeation is therefore remarkably smaller than that of H₂, enhancing the H₂/CH₄ selectivity. Last, both H₂ and CH₄ cannot permeate the interfacial space between graphene and the (010) face of MFI, because of the less uneven surface structures than the (100) face. In-pore permeation, which can be observed in trajectories projected to the *ac* plane, is thus the only possible path (Fig. 4, G₁ and G₂). H₂ and CH₄ permeation pathways projected onto the *bc* plane are consequently different from each other. H₂ molecules permeate through both the interfacial spaces between graphene and the (100) face and the MFI pores, whereas CH₄ permeates only through the MFI pores. Hence, H₂ molecules can bypass at the interfacial spaces and permeate faster than CH₄ molecules. The important role of the interfacial bypass in the permeation of H₂ was confirmed by the trajectory length. The average trajectory length of H₂ molecules passing through the G-MFI (1170 nm) was 420 nm shorter than the average trajectory length of CH₄ (1590 nm).

The time course of H₂ and CH₄ potential energy from the feed to permeate through G-MFI is shown in Fig. 4 (H and I). The potential energy of noninteracted H₂ or CH₄ in the gas phase as feed and permeate was set as 0 kJ mol⁻¹. H₂ or CH₄ attractively interacts with pores of MFI and/or interfacial spaces, and thus the permeation time of H₂ or CH₄ in G-MFI can be determined by the duration of the negative potential energy zone (−0.2 kJ mol⁻¹ for H₂ and −0.6 kJ mol⁻¹ for CH₄), although repulsive collisions cause positive spikes in the potential energy. The feed is characterized by higher positive energy fluctuations than the permeate molecules, owing to the higher density of the inlet gas.

The total permeation time can be determined from potential energy/time graphs. H₂ total permeation time through the nanoscale model membrane (0.7 ns) is five times shorter than that of CH₄ (3.6 ns). The high permeation selectivity of G-MFI for H₂ for the adopted nanoscale model further broadens at a micrometer level. Therefore, the permeation of H₂ molecules through the bypass in the G-MFI membrane film can give a selectivity of H₂/CH₄ nearly 100 for a single gas.

The permeance of H₂ decreases with the length of the model crystal (Fig. 5A). The interfacial space between graphene and MFI crystal face is the key for molecular sieving, as confirmed by simulation of the H₂ and CH₄ permeance through the MFI crystal (fig. S10, E and F). The H₂ permeance through the G-MFI is smaller than that through the MFI model due to difference in the pore structure between MFI and G-MFI. The MFI has the pores of 0.55 nm, while the model structure of G-MFI has the interfacial 2D pores (Fig. 4, C and D) of 0.369 nm. The small 2D interfacial pores produced by graphene wrapping serve as the energy barriers for CH₄, being responsible for molecular sieving (Fig. 4D). The larger interfacial area suggests that there are more energy barriers for H₂ at the graphene-MFI interfacial spaces, affecting H₂ permeability. The permeability reduction for CH₄ was more prominent for the larger interfacial surface membranes. Accordingly, the selectivity for single gas and mixed gas increased with an increase in the interfacial area of the membrane (Fig. 5B). The synthesized G-MFI membrane can be regarded as an extreme case of model membranes. The G-MFI membrane is 150 μm thick; thus, the number of interfacial

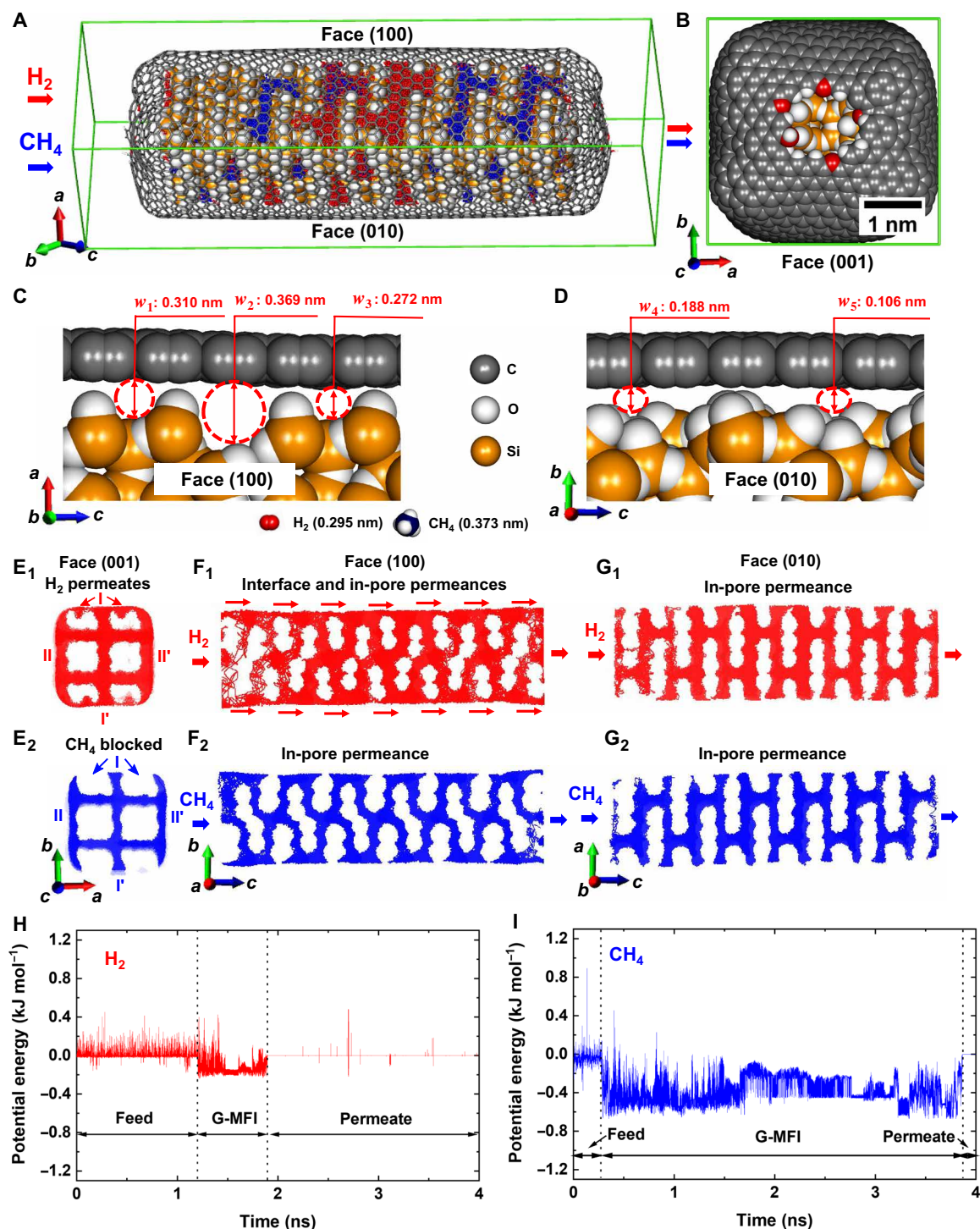


Fig. 4. Permeability mechanism through the G-MFI crystal rod membrane model. (A) Permeation trajectories of H_2 in red color and CH_4 in blue color along the (100) and (010) MFI crystal faces of G-MFI crystal rod model. (B) Nanowindow on graphene contacted with the (001) MFI crystal face; surface oxygen atoms are in red. (C) Interface between graphene and (100) MFI crystal face. (D) Interface between graphene and (010) MFI crystal face. (E₁ and E₂) Trajectories of H_2 and CH_4 projected (001) face. The trajectories at the sides are denoted as I, I', II, and II', representing permeation at the graphene-MFI interfacial spaces. (F₁ and F₂) Trajectories projected to (100) face. Red arrows show permeation of H_2 at the graphene-MFI interfacial spaces. Blue trajectory of CH_4 shows that CH_4 permeates through the pores, but not through the graphene-MFI interfacial spaces. (G₁ and G₂) Trajectories projected to (010) face, showing that H_2 and CH_4 permeate through the pores of MFI crystal. (H and I) Time courses of the potential energy of H_2 and CH_4 .

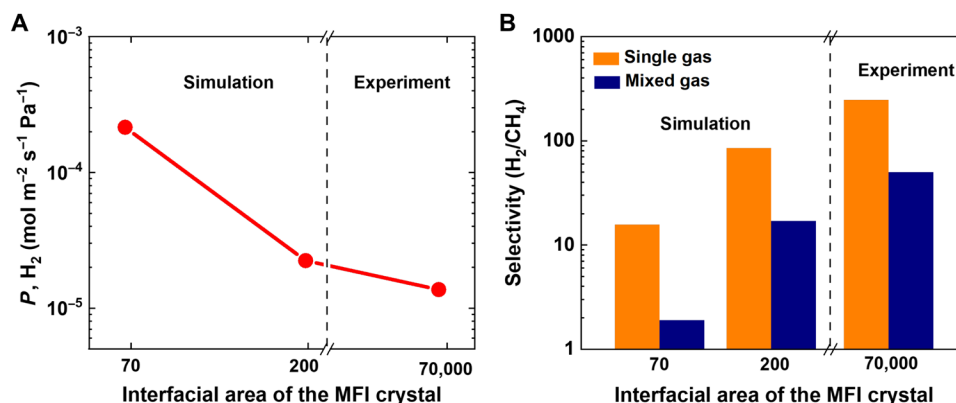


Fig. 5. G-MFI permeability and selectivity. (A) H₂ permeability plotted against the interfacial surface area of the MFI crystal, as determined by simulations and experiments. (B) H₂/CH₄ selectivity plotted against the interfacial surface area of the MFI crystal, as determined by simulations and experiments for single and mixed gases. Interfacial area is equal to the geometrical external area of MFI crystal for simulation and MFI particles for experiment.

contacts between graphene and MFI crystals, which act as energy barriers, is considerable, resulting in higher experimental selectivity.

DISCUSSION

G-MFI membranes efficiently separate H₂ with high selectivity at an ultrahigh permeability of ~10⁶ barrers, due to both the narrow micropore spaces between graphene and zeolite crystal surface and the hierarchical pore structure. The activation energy for H₂ permeation through the G-MFI membrane was 9.5 kJ mol⁻¹ (fig. S11), supporting that the molecular sieving effect is due to narrow micropores, in agreement with the MD simulations. We examined the effect of zeolite crystal face effect on permeability. The graphene-wrapped BEA zeolite membrane had a significantly higher permeability than G-MFI, but almost no H₂/CH₄ selectivity (fig. S12). This is because the width of the interfacial space of the graphene-wrapped BEA zeolite is larger than the molecular size of H₂ and CH₄. Thus, the interfacial space should induce the observed molecular sieving effect of G-MFI for H₂.

The G-MFI membrane is stable over 7 days, during which the selectivity of 50 for separation of an equimolar H₂/CH₄ mixture is maintained. The preparation of the crack-free G-MFI membrane via the illustrated facile route can be applied to highly efficient and economic H₂ separation processes. The G-MFI membrane satisfies the requirements of the flux of 1.05 mol m⁻² s⁻¹ for efficient industrial separation (37); the flux of H₂ through G-MFI membrane was measured to be 1.3 mol m⁻² s⁻¹. The graphene-wrapping methodology can be extended to the design of novel and highly performant separation membranes for any target gas, to ultimately promote a breakthrough toward green technologies.

MATERIALS AND METHODS

Wrapping of MFI zeolites with graphene and membrane preparation

Graphene wrapping of MFI zeolites was carried out in the colloidal state using GO and silicalite-1 (MFI zeolites) as raw materials. MFI crystals were synthesized by the sol-gel method, yielding a particle size of 300 nm (38). A solution consisting of tetrapropylammonium (TPA) hydroxide, sodium hydroxide, and distilled water at the

stoichiometric ratio of 25 SiO₂:2 (TPA)₂O:1100 H₂O:100 C₂H₅OH:0.1 Na₂O was mixed at 298 K for 30 min (38). Tetraethyl orthosilicate was slowly added to the reaction mixture and stirred at 298 K for 24 hours. The reaction mixture was poured into a Teflon-lined autoclave and hydrothermally treated at 373 K for 24 hours. After hydrothermal treatment, white precipitation was obtained via filtration. The filtered powder was washed using boiling water and dried at 383 K. The MFI-type zeolite powder was calcined in air atmosphere at 773 K for 8 hours to remove organic structure-directing agents. GO was synthesized following the modified Hummers' method (39). Madagascar graphite (5 g) was placed in a 1-liter beaker on a hot plate with a magnetic stirrer and thermometer. The magnetic stirring was set at 150 rpm. We slowly added 200 ml of concentrated H₂SO₄ and 22 ml of concentrated H₃PO₄, followed by 25 g of KMnO₄, while maintaining a temperature of 308 to 313 K. The stirring speed was increased to 300 rpm and the reaction lasted for 5 hours. After the reaction, the beaker with the reaction mixture was placed in a plastic bowl containing ice, and 500 ml of water was slowly added, maintaining a temperature of <313 K. Then, 100 ml of H₂O₂ (10%) was slowly added. The GO was washed with 5% HCl five times to remove the remaining metal impurities. Last, the remaining acid was washed five times with water. The washed metals and acids were separated from GO by centrifugation. The GO was washed five times in water to exfoliate graphene sheets, and a diluted GO supernatant was collected.

The amount of GO was estimated to be sufficient for a single-layer wrapping of the external surface area of the MFI crystals (62 m² g⁻¹). Since the interactions between the MFI crystals and GO are weak in aqueous solution, we enhanced the interactions between the GO and MFI crystals by adding NH₄Cl, which dissociates into NH₄⁺ and Cl⁻ ions. NH₄⁺ protonates the carboxyl functional groups, decreasing the surface energy or zeta potential of the GO layers and, thereby, facilitating the shrinking and wrapping process (40). An experimental flowchart for the wrapping of the MFI crystal with GO is shown in fig. S1.

We wrapped MFI zeolites with GO colloids (fig. S1A) by combining 50 mg of MFI zeolite crystals and 4.6 ml of a GO dispersion with a mass concentration of 0.04 weight % GO. We added 20 ml of 0.1 M NH₄Cl to enhance interactions between the MFI and GO. After 24 hours, the GO enveloped the MFI crystals, leading to precipitation.

We then froze the GO-wrapped MFI crystals with liquid nitrogen and removed frozen water with a freeze dryer to obtain the GO-wrapped MFI crystals (fig. S1B). The GO-wrapped MFI was thermally treated at a heating rate of 1 K min^{-1} in Ar at 623 K for 10 min to yield a G-MFI powder-like material, which was used for the fabrication of G-MFI membranes (fig. S1C).

The membrane was prepared by compression of G-MFI powder into a pellet using a compression die at a pressure of 550 MPa for 15 min. Compression yielded a 6-mm^2 membrane (fig. S1, G to J). The size of the die used for making the membrane was 6 mm by 6 mm. We used 10 mg of G-MFI powder for membrane preparation using the die compression method. Using araldite adhesive, the membrane was mounted onto a polyacrylate plate holder with a 1-mm-diameter hole at the center.

MD simulation

Classical MD simulations were conducted to elucidate the gas permeation mechanism through G-MFI membrane. We used large-scale atomic/molecular massively parallel simulator (LAMMPS) (41) to simulate the permeation of H_2 and CH_4 molecules. The H_2 and CH_4 molecules were set as single uncharged Lennard-Jones (LJ) centers, and the force field parameters are given in table S5. We conducted single and mixed gas permeance simulations with 1000 molecules in the simulation box. Equimolar mixture of H_2 and CH_4 was used for the mixed gas simulations. Periodic boundary conditions in the a and b directions were applied. The dimensions of the box in the a and b directions were set according to the size of the G-MFI model. The LJ 9-3 potential walls perpendicular to the c axis having small energy parameter were set at $c = -300\text{ nm}$ and $c = 50\text{ nm}$. The G-MFI model was set at the origin in the coordinate system. The simulations were conducted at 298.15 K and the time step was 1 fs. The Nosé-Hoover thermostat was used to control the temperature. The total number of timesteps was 3×10^6 (3 ns), which was enough time for H_2 and CH_4 permeance. We recorded the number of molecules permeated through the model G-MFI membrane every 50 MD steps.

We constructed a G-MFI membrane model based on an MFI crystal wrapped with graphene. We used the orthorhombic MFI crystal unit with lattice constants of $a = 2.0090\text{ nm}$, $b = 1.9738\text{ nm}$, and $c = 1.3142\text{ nm}$ (42). We constructed the MFI crystal rod by extending the MFI crystal unit along the c axis. Si atoms in MFI were terminated with O atoms. The G-MFI model was built with packmol (43). The graphene layers were connected at the edges, and partial structural relaxation was performed for the edge parts using a discovery studio visualizer. Nanowindows of $\sim 1\text{ nm}$ in diameter were opened at the center of both ends of the G-MFI rod model. After wrapping, the whole graphene structure was relaxed using the ReaxFF potential implemented in LAMMPS for the structural relaxation of the graphene structure.

MFI crystal rod models were used to calculate the permeance of the H_2 and CH_4 molecules. The effect of the crystal rod length on H_2 and CH_4 permeation through G-MFI was examined using 7.885- and 43.368-nm-long MFI crystals (fig. S7). The effective distance between graphene and MFI crystalline surface was set at 0.03 nm. An effect of the effective width on the permeation was examined using a 7.885-nm-long MFI crystal; the effective widths between graphene and the MFI crystal were 0.030, 0.30, and 0.40 nm (fig. S10).

We calculated the number of permeated molecules against time for each G-MFI rod model; the slope of the permeated molecules against time was found to be proportional to the molar flow in units

of moles per second of the molecules through the G-MFI rod crystal. Dividing the molar flow in units of moles per second with the area of the G-MFI rod in units of square meters and transmembrane pressure difference in units of pascals gives the permeance expressed in units of moles per square meter per second per pascal. We used the areas of 10.60, 12.57, and 17.28 nm^2 and the effective widths of 0.030, 0.30, and 0.40 nm, respectively, for calculation of the permeance. The transmembrane pressures were 8.4, 7.1, and 5.2 MPa for the effective widths of 0.030, 0.30, and 0.40 nm, respectively. High transmembrane pressures were used to determine the permeance with high statistical accuracy to obtain sufficient permeated molecules within the calculation time of a few hundreds of nanoseconds. The permeance was evaluated as expressed by the following equation

$$\text{Permeance} = N/(A \cdot t \cdot \Delta P) \quad (1)$$

where N denotes the number of permeated molecules, A is the area of the membrane, t is the time for molecules to permeate, and ΔP is the transmembrane pressure. We ran the simulation five times for each model and calculated the average permeances and selectivities.

Explanation of effective width used in MD simulation

The effective width (w) is defined as follows

$$w = H - 0.322\text{ (nm)} \quad (2)$$

where H is the internuclear distance between the carbon atom in graphene and the oxygen atom on the outermost surface of the MFI crystal. A parameter of 0.322 nm corresponds to the sum of the van der Waals radii of a solid carbon atom in graphene and an oxygen atom in the MFI crystal.

SUPPLEMENTARY MATERIALS

Supplementary material for this article is available at <https://science.org/doi/10.1126/sciadv.abl3521>

REFERENCES AND NOTES

1. N. Sazali, M. A. Mohamed, W. N. W. Salleh, Membranes for hydrogen separation: A significant review. *Int. J. Adv. Manuf. Technol.* **107**, 1859–1881 (2020).
2. Q. Qian, P. A. Asinger, M. J. Lee, G. Han, K. M. Rodriguez, S. Lin, F. M. Benedetti, A. X. Wu, W. S. Chi, Z. P. Smith, MOF-based membranes for gas separations. *Chem. Rev.* **120**, 8161–8266 (2020).
3. R. Magnus, A. Lyngfelt, Using steam reforming to produce hydrogen with carbon dioxide capture by chemical-looping combustion. *International journal of hydrogen energy*. *Int. J. Hydrog.* **31**, 1271–1283 (2006).
4. N. W. Ockwig, T. M. Nenoff, Membranes for hydrogen separation. *Chem. Rev.* **107**, 4078–4110 (2007).
5. R. Ullah, M. Khraisheh, R. J. Esteves, J. T. McLeskey, M. AlGhouti, M. Gad-el-Hak, H. V. Tafreshi, Energy efficiency of direct contact membrane distillation. *Desalination* **433**, 56–67 (2018).
6. C. Lastoskie, Caging carbon dioxide. *Science* **330**, 595–596 (2010).
7. D. S. Sholl, R. P. Lively, Seven chemical separations to change the world. *Nature* **532**, 435–437 (2016).
8. E. M. Flanigen, J. M. Bennett, R. W. Grose, J. P. Cohen, R. L. Patton, R. M. Kirchner, J. V. Smith, Silicalite, a new hydrophobic crystalline silica molecular sieve. *Nature* **271**, 512–516 (1978).
9. K. Varoon, X. Zhang, B. Elyassi, D. D. Brewer, M. Gettel, S. Kumar, A. Lee, S. Maheshwari, A. Mittal, C. Y. Sung, M. Cococcioni, L. F. Francis, A. V. McCormick, K. A. Mkhoyan, M. Tsapatsis, Dispersible exfoliated zeolite nanosheets and their application as a selective membrane. *Science* **334**, 72–75 (2011).
10. M. Dakhchoune, L. F. Villalobos, R. Semino, L. Liu, M. Rezaei, P. Schouwink, C. E. Avalos, P. Baade, V. Wood, Y. Han, M. Ceriotti, K. V. Agrawal, Gas-sieving zeolitic membranes fabricated by condensation of precursor nanosheets. *Nat. Mater.* **20**, 362–369 (2021).

11. G. Bernardo, T. Araújo, T. da Silva Lopes, J. Sousa, A. Mendes, Recent advances in membrane technologies for hydrogen purification. *Int. J. Hydrogen Energy* **45**, 7313–7338 (2020).
12. Z. Tang, J. Dong, T. M. Nenoff, Internal surface modification of MFI-type zeolite membranes for high selectivity and high flux for hydrogen. *Langmuir* **25**, 4848–4852 (2009).
13. H. Wang, Y. S. Lin, Synthesis and modification of ZSM-5/silicalite bilayer membrane with improved hydrogen separation performance. *J. Memb. Sci.* **396**, 128–137 (2012).
14. T. S. Chung, L. Y. Jiang, Y. Li, S. Kulprathipanja, Mixed matrix membranes (MMMs) comprising organic polymers with dispersed inorganic fillers for gas separation. *Prog. Polym. Sci.* **32**, 483–507 (2007).
15. L. Cheng, G. Liu, J. Zhao, W. Jin, Two-dimensional-material membranes: Manipulating the transport pathway for molecular separation. *Accounts Mater. Res.* **2**, 114–128 (2021).
16. B. Zornoza, O. Esekile, W. J. Koros, C. Téllez, J. Coronas, Hollow silicalite-1 sphere-polymer mixed matrix membranes for gas separation. *Sep. Purif. Technol.* **77**, 137–145 (2011).
17. H. Verweij, Inorganic membranes. *Curr. Opin. Chem. Eng.* **1**, 156–162 (2012).
18. F. V.-Burgos, F. X. Coudert, K. Kaneko, Air separation with graphene mediated by nanowindow-rim concerted motion. *Nat. Commun.* **9**, 1812 (2018).
19. D. Stevic, A. Furuse, F. V.-Burgos, R. Kukobat, K. Kaneko, Cu-phthalocyanine-mediated nanowindow production on single-wall carbon nanohorn. *Mol. Phys.* **119**, e1815883 (2021).
20. K. Murata, K. Hirahara, M. Yudasaka, S. Iijima, D. Kasuya, K. Kaneko, Nanowindow-induced molecular sieving effect in a single-wall carbon nanohorn. *J. Phys. Chem. B* **106**, 12668–12669 (2002).
21. Z. Lu, M. L. Dunn, Van der Waals adhesion of graphene membranes. *J. Appl. Phys.* **107**, 044301 (2010).
22. D. D. L. Chung, Review: Graphite. *J. Mater. Sci.* **37**, 1475–1489 (2002).
23. M. Sakai, T. Kaneko, Y. Sasaki, M. Sekigawa, M. Matsukata, Formation process of columnar grown (101)-oriented silicalite-1 membrane and its separation property for xylene isomer. *Crystals* **10**, 949 (2020).
24. J. Dong, K. Wegner, Y. S. Lin, Synthesis of submicron polycrystalline MFI zeolite films on porous ceramic supports. *J. Memb. Sci.* **148**, 233–241 (1998).
25. U. Beuscher, E. J. Kappert, J. G. Wijmans, Membrane research beyond materials science. *J. Membr. Sci.* **643**, 119902 (2022).
26. Y. Jeong, S. Kim, M. Lee, S. Hong, M. G. Jang, N. Choi, K. S. Hwang, H. Baik, J. K. Kim, A. Yip, J. Choi, A hybrid zeolite membrane-based breakthrough for simultaneous CO₂ capture and CH₄ upgrading from biogas. *ACS Appl. Mater. Interfaces* **14**, 2893–2907 (2022).
27. S. Wang, Y. Yoshikawa, Z. Wang, H. Tanaka, K. Kaneko, Highly oxidation-resistant graphene-based porous carbon as a metal catalyst support. *Carbon Trends* **3**, 100029 (2021).
28. I. Diaz, E. Kokkoli, O. Terasaki, M. Tsapatsis, Surface structure of zeolite (MFI) crystals. *Chem. Mater.* **16**, 5226–5232 (2004).
29. R. T. Ferrel, D. M. Himmelbau, Diffusion coefficients of hydrogen and helium in water. *AIChE J.* **13**, 702–798 (1967).
30. P. L. Llewellyn, J. P. Coulomb, Y. Grillet, J. Patarin, G. Andre, J. Rouquerol, Adsorption by MFI-type zeolites examined by isothermal microcalorimetry and neutron diffraction. 2. nitrogen and carbon monoxide. *Langmuir* **9**, 1852–1856 (1993).
31. U. Müller, K. K. Unger, Sorption studies on large ZSM-5 crystals: The influence of aluminium content, the type of exchangeable cations and the temperature on nitrogen hysteresis effects. *Charact. Porous Solids* **39**, 101–108 (1988).
32. N. Setoyama, M. Ruike, T. Kasu, T. Suzuki, K. Kaneko, Surface characterization of microporous solids with helium adsorption and small angle x-ray scattering. *Langmuir* **9**, 2612–2617 (1993).
33. I. Mitxelena, M. Piris, Molecular electric moments calculated by using natural orbital functional theory. *J. Chem. Phys.* **144**, 204108 (2016).
34. K. S. W. Sing, R. T. Williams, The use of molecular probes for the characterization of nanoporous adsorbents. *Part. Part. Syst. Charact.* **21**, 71–79 (2004).
35. M. A. Carreon, S. Li, J. L. Falconer, R. D. Noble, Alumina-supported SAPO-34 membranes for CO₂/CH₄ separation. *J. Am. Chem. Soc.* **130**, 5412–5413 (2008).
36. T. Ohba, T. Suzuki, K. Kaneko, Preformed monolayer-induced filling of molecules in micropores. *Chem. Phys. Lett.* **326**, 158–162 (2000).
37. J. W. Phair, R. Donelson, Developments and design of novel (non-palladium-based) metal membranes for hydrogen separation. *Ind. Eng. Chem. Res.* **45**, 5657–5674 (2006).
38. N. Ren, Z. J. Yang, X. C. Lv, J. Shi, Y. H. Zhang, Y. Tang, A seed surface crystallization approach for rapid synthesis of submicron ZSM-5 zeolite with controllable crystal size and morphology. *Microporous Mesoporous Mater.* **131**, 103–114 (2010).
39. D. C. Marcano, D. V. Kosynkin, J. M. Berlin, A. Sinitskii, Z. Sun, A. Slesarev, L. B. Alemany, W. Lu, J. M. Tour, Improved synthesis of graphene oxide. *ACS Nano* **4**, 4806–4814 (2010).
40. J. Rong, M. Ge, X. Fang, C. Zhou, Solution ionic strength engineering as a generic strategy to coat graphene oxide (GO) on various functional particles and its application in high-performance lithium-sulfur (Li-S) batteries. *Nano Lett.* **14**, 473–479 (2014).
41. A. P. Thompson, H. M. Aktulga, R. Berger, D. S. Bolintineanu, W. M. Brown, P. S. Crozier, P. J. in 't Veld, A. Kohlmeyer, S. G. Moore, T. D. Nguyen, R. Shan, M. J. Stevens, J. Tranchida, C. Trott, S. J. Plimpton, LAMMPS - A flexible simulation tool for particle-based materials modeling at the atomic, meso, and continuum scales. *Comp. Phys. Comm.* **271**, 10817 (2022).
42. Database of Zeolite Structures (2017). Structure Commission of the International Zeolite Association (IZA-SC), Retrieved from <http://www.iza-structure.org/databases/>.
43. L. Martínez, R. Andrade, E. G. Birgin, J. M. Martínez, PACKMOL: A graphical user interface for computational chemistry softwares. *J. Comput. Chem.* **30**, 2157–2164 (2009).
44. L. M. Robeson, The upper bound revisited. *J. Memb. Sci.* **320**, 390–400 (2008).
45. A. F. Ismail, K. C. Khulbe, T. Matsuura, *Gas Separation Membranes: Polymeric and Inorganic* (Springer International Publishing, 2015).
46. R. M. de Vos, H. Verwelj, High-selectivity, high-flux silica membranes for gas separation. *Science* **279**, 1710–1711 (1998).
47. B. Elyassi, M. Sahimi, T. T. Tsotsis, Silicon carbide membranes for gas separation applications. *J. Memb. Sci.* **288**, 290–297 (2007).
48. S. Li, J. L. Falconer, R. D. Noble, SAPO-34 membranes for CO₂/CH₄ separations: Effect of Si/Al ratio. *Microporous Mesoporous Mater.* **110**, 310–317 (2008).
49. H. Guo, G. Zhu, J. J. Hewitt, S. Qiu, "Twin copper source" growth of metal-organic framework membrane: Cu₃(BTC)₂ with high permeability and selectivity for recycling H₂. *J. Am. Chem. Soc.* **131**, 1646–1647 (2009).
50. Y. Li, F. Liang, H. Bux, W. Yang, J. Caro, Zeolitic imidazolate framework ZIF-7 based molecular sieve membrane for hydrogen separation. *J. Memb. Sci.* **354**, 48–54 (2010).
51. H. Li, Z. Song, X. Zhang, Y. Huang, S. Li, Y. Mao, H. J. Ploehn, Y. Bao, M. Yu, Ultrathin, Molecular-sieving graphene oxide membranes for selective hydrogen separation. *Science* (80). **342**, 95–98 (2013).
52. S. Zhou, X. Zou, F. Sun, H. Ren, J. Liu, F. Zhang, N. Zhao, G. Zhu, Development of hydrogen-selective CAU-1 MOF membranes for hydrogen purification by "dual-metal-source" approach. *Int. J. Hydrogen Energy* **38**, 5338–5347 (2013).
53. X. Zhang, Y. Liu, S. Li, L. Kong, H. Liu, Y. Li, W. Han, K. L. Yeung, W. Zhu, W. Yang, J. Qiu, New membrane architecture with high performance: ZIF-8 membrane supported on vertically aligned ZnO nanorods for gas permeation and separation. *Chem. Mater.* **26**, 1975–1981 (2014).
54. A. Huang, Q. Liu, N. Wang, Y. Zhu, Bicontinuous ZIF-8@GO membrane with enhanced hydrogen selectivity. *J. Am. Chem. Soc.* **136**, 14686–14689 (2014).
55. D. Wang, Z. Wang, L. Wang, L. Hu, J. Jin, Ultrathin membranes of single-layered MoS₂ nanosheets for high-permeance hydrogen separation. *Nanoscale* **7**, 17649–17652 (2015).
56. J. Fu, S. Das, G. Xing, T. Ben, V. Valtchev, S. Qiu, Fabrication of COF-MOF composite membranes and their highly selective separation of H₂/CO₂. *J. Am. Chem. Soc.* **138**, 7673–7680 (2016).
57. A. Achari, S. Sahana, M. Eswaramoorthy, High performance MoS₂ membranes: Effects of thermally driven phase transition on CO₂ separation efficiency. *Energ. Environ. Sci.* **9**, 1224–1228 (2016).
58. Z. Wang, D. Wang, S. Zhang, L. Hu, J. Jin, Interfacial design of mixed matrix membranes for improved gas separation performance. *Adv. Mater.* **28**, 3399–3405 (2016).
59. Q. Zhang, S. Luo, J. R. Weidman, R. Guo, Preparation and gas separation performance of mixed-matrix membranes based on triptycene-containing polyimide and zeolite imidazole framework (ZIF-90). *Polymer (Guildf)*. **131**, 209–216 (2017).
60. L. Ding, Y. Wei, L. Li, T. Zhang, H. Wang, J. Xue, L. X. Ding, S. Wang, J. Caro, Y. Gogotsi, MXene molecular sieving membranes for highly efficient gas separation. *Nat. Commun.* **9**, 155 (2018).
61. M. Guo, M. Kanezashi, H. Nagasawa, L. Yu, J. Ohshita, T. Tsuru, Amino-decorated organosilica membranes for highly permeable CO₂ capture. *J. Memb. Sci.* **611**, 118328 (2020).
62. S. Araki, Y. Okubo, K. Maekawa, S. Imasaka, H. Yamamoto, Preparation of a high-silica chabazite-type zeolite membrane with high CO₂ permeability using tetraethylammonium hydroxide. *J. Memb. Sci.* **613**, 118480 (2020).
63. S. Huang, S. Li, L. F. Villalobos, M. Dakhchoune, M. Micari, D. J. Babu, M. T. Vahdat, M. Mensi, E. Oveis, K. V. Agrawal, Millisecond lattice gasification for high-density CO₂- and O₂-sieving nanopores in single-layer graphene. *Sci. Adv.* **7**, eabf0116 (2021).
64. H. Fan, M. Peng, I. Strauss, A. Mundstock, H. Meng, J. Caro, MOF-in-COF molecular sieving membrane for selective hydrogen separation. *Nat. Commun.* **12**, 38 (2021).
65. L. Lei, F. Pan, A. Lindbräthen, X. Zhang, M. Hillestad, Y. Nie, L. Bai, X. He, M. D. Guiver, Carbon hollow fiber membranes for a molecular sieve with precise-cutoff ultramicropores for superior hydrogen separation. *Nat. Commun.* **12**, 268 (2021).
66. S. Brunauer, P. H. Emmett, E. Teller, Adsorption of gases in multimolecular layers. *J. Am. Chem. Soc.* **60**, 309–319 (1938).

67. K. Kaneko, C. Ishii, M. Ruike, H. Kuwabara, Origin of superhigh surface area and microcrystalline graphitic structures of activated carbons. *Carbon N. Y.* **30**, 1075–1088 (1992).
68. P. V. Konarev, V. V. Volkov, A. V. Sokolova, M. H. J. Koch, D. I. Svergun, PRIMUS: A windows PC-based system for small-angle scattering data analysis. *J. Appl. Cryst.* **36**, 1277–1282 (2003).
69. K. S. Deeg, J. J. G.-Sevillano, R. B.-Pérez, J. B. Parra, C. O. Ania, M. Doblaré, S. Calero, Insights on the molecular mechanisms of hydrogen adsorption in zeolites. *J. Phys. Chem. C* **117**, 14374–14380 (2013).
70. M. G. Martin, J. I. Siepmann, Transferable potentials for phase equilibria. 1. United-atom description of *n*-alkanes. *J. Phys. Chem. B* **102**, 2569–2577 (1998).
71. B. Vujic, A. P. Lyubartsev, Transferable force-field for modelling of CO₂, N₂, O₂ and Ar in all silica and Na⁺ exchanged zeolites. *Model. Simul. Mater. Sci. Eng.* **24**, 045002 (2016).

Acknowledgments: We are grateful to M. Yoshimune (AIST) for comments and suggestions.

Funding: This work was supported by Japan Science Technology Agency (JST) CREST project

“Creation of Innovative Functional Materials with Advanced Properties by Hyper-Nanospace Design”; Japan Science Technology Agency (JST) Open Innovation Platform with Enterprise, Research Institute and Academia (OPERA) (JPMJOP1722); and TAKAGI Co. Ltd. **Author contributions:** Membrane preparation: R.K. Gas permeance measurements: M.S. MD simulations: R.K. and H.T. Gas adsorption measurements: R.K. and H.O. TEM observations: T.H., Y.S., and K.Y. Writing—original draft: R.K. and K.K. Writing—review and editing: R.K., K.K., F.V.-B., C.L., and M.M. **Competing interests:** R.K., F.V.-B., and K.K. are inventors on a patent related to this work filed by National Cooperation University Shinshu University and Kotobuki Holdings Co. Ltd. (no. P690172, published 22 June 2021). The authors declare that they have no other competing interests. **Data and materials availability:** All data needed to evaluate the conclusions in the paper are present in the paper and/or the Supplementary Materials.

Submitted 8 July 2021

Accepted 1 April 2022

Published 18 May 2022

10.1126/sciadv.abl3521

Ultrapermeable 2D-channelled graphene-wrapped zeolite molecular sieving membranes for hydrogen separation

Radovan Kukobat, Motomu Sakai, Hideki Tanaka, Hayato Otsuka, Fernando Vallejos-Burgos, Christian Lastoskie, Masahiko Matsukata, Yukichi Sasaki, Kaname Yoshida, Takuya Hayashi, and Katsumi Kaneko

Sci. Adv., **8** (20), eabl3521.
DOI: 10.1126/sciadv.abl3521

View the article online

<https://www.science.org/doi/10.1126/sciadv.abl3521>

Permissions

<https://www.science.org/help/reprints-and-permissions>

Use of this article is subject to the [Terms of service](#)